Trajectory Planning of Cellular-Connected UAV for Communication-assisted Radar Sensing

Shuyan Hu, *Member, IEEE*, Xin Yuan, *Member, IEEE*, Wei Ni, *Senior Member, IEEE*, and Xin Wang, *Senior Member, IEEE*

Abstract—**Being a key technology for beyond fifth-generation wireless systems, joint communication and radar sensing (JCAS) utilizes the reflections of communication signals to detect foreign objects and deliver situational awareness. A cellular-connected unmanned aerial vehicle (UAV) is uniquely suited to form a mobile bistatic synthetic aperture radar (SAR) with its serving base station (BS) to sense over large areas with superb sensing resolutions at no additional requirement of spectrum. This paper designs this novel BS-UAV bistatic SAR platform, and optimizes the flight path of the UAV to minimize its propulsion energy and guarantee the required sensing resolutions on a series of interesting landmarks. A new trajectory planning algorithm is developed to convexify the propulsion energy and resolution requirements by using successive convex approximation and block coordinate descent. Effective trajectories are obtained with a polynomial complexity. Extensive simulations reveal that the proposed trajectory planning algorithm outperforms significantly its alternative that minimizes the flight distance of cellular-aided sensing missions in terms of energy efficiency and effective consumption fluctuation. The energy saving offered by the proposed algorithm can be as significant as 55%.**

Index Terms—**Joint communication and radar sensing, bistatic synthetic aperture radar, cellular-connected unmanned aerial vehicle, block coordinate descent.**

I. INTRODUCTION

Recent advancements in the fifth-generation and beyond (5G/B5G) networks are increasingly enabling extensive background situation- and position-aware smart applications, including autonomous driving, distant medical care, and smart industry [1]. 5G/B5G networks are also envisioned to offer high-resolution sensing in support of these applications [2]. For this reason, joint communication and radar sensing (JCAS) has been deemed as one of the essential technologies in 5G/B5G systems [3]. By integrating radio communication and sensing into a single system, JCAS measures the reflections of communication signals to sense the location, velocity, and feature signal of targets and motions [4], [5]. This is

Shuyan Hu and Xin Yuan contributed equally to this work. (Corresponding author: Xin Wang.)

S. Hu is with the Key Lab of EMW Information (MoE), the School of Information Science and Technology, Fudan University, Shanghai 200433, China (e-mail: syhu14@fudan.edu.cn).

X. Yuan and W. Ni are with the Data61, Commonwealth Scientific and Industrial Research Organization, Sydney, NSW 2122, Australia (e-mails: {xin.yuan, wei.ni}@data61.csiro.au).

X. Wang is with the Key Lab of EMW Information (MoE), the Department of Communication Science and Engineering, Fudan University, Shanghai 200433, China (e-mail: xwang11@fudan.edu.cn).

different from the widely accessible Global Positioning System (GPS), which enables every GPS receiver to locate itself by correlating the preambles/pilots from multiple (four or more) satellites [6], [7]. Neither of the GPS satellites and ground receivers sense the environment or deliver situational awareness, as opposed to JCAS [3].

Cellular-connected unmanned aerial vehicles (UAVs) have been increasingly considered for their operability and applicability to UAV operations over wide areas [8], [9]. Apart from being an aerial user of communication services, a cellular-connected UAV can potentially utilize the cellular signals from corresponding base stations (BSs), and collect the echo signals from the ground (e.g., metallic) objects to perform radar sensing in areas covered by the BSs. Given the excellent mobility, the UAV can potentially form a bistatic synthetic aperture radar (SAR) with its serving BS to sense the environment. While dedicated sensing or radar techniques may detect objects with even better resolution (e.g., because of their wider signal bandwidth and higher signal power), they inevitably bring radio radiation and pollution [3]. Nevertheless, the UAVs are passive receivers, and neither increase the radio footprint of the system nor produce radio pollution.

Fig. 1 illustrates the new cellular-assisted radar sensing by a cellular-connected UAV, referred to as BS-UAV bistatic SAR sensing, where the reflections of the downlink cellular signals are picked up by the UAV and used to produce radio/radar images for object detection. Since the UAV is typically power-constrained, it is critical to carefully plan its trajectory to deliver energy-efficient radar sensing missions and extend mission time. Existing works have only designed the trajectory to minimize the UAV propulsion energy for wireless communication services, such as [10]–[13]. None has considered the energy consumption in the new scenario of cellular-assisted radar sensing with a cellular-connected UAV.

A. Related Work

Existing studies of JCAS systems have typically focused on the beamforming design at the BSs, and have not considered the use of a UAV. These JCAS systems are in essence monostatic radars, which integrate the transmitter and receiver on the same platform. In [14], waveform design was optimized to confirm the produced signal to the expected sensing waveform subject to the signal-to-interference-and-noise ratio (SINR) requirement for multiuser multiple-input multiple-output (MIMO) communications. In [15], globally optimal waveforms were devised for several expected sensing

beam patterns to minimize multiuser interference. In [16], a multibeam technique was introduced for millimeter-wave (mmWave) JCAS with analog antenna arrays, and a fixed transmission subbeam was produced together with direction-changing scanning subbeams across various packets. In [17], a multi-metric waveform was designed for multiple-input single-output (MISO) communications to maximize the SINR at the users. On the other hand, a higher signal power is typically on demand for high-resolution sensing over long ranges, whereas the BSs usually have a limited transmit power. The sensing performance may considerably degrade if the targets are far away from the BS, because of the significant round-trip path loss attenuation of the echoed signals.

UAVs have been emerging as a new type of passive receiver in bistatic radar systems. Unlike a monostatic radar, a bistatic radar uses geographically separated antennas for signal transmission and reception. The German TanDEM-X project (initiated in June 2010) developed the first prototype of a space-borne bistatic radar, relying on twin low-Earth-orbiting (LEO) satellites traveling in near formation [18]. The High-Resolution Wide-Swath (HRWS) project was proposed to be the next-generation German space-borne radar platform for geological and geographical observation beyond 2030, by leveraging the formation movement of an active satellite and three passive satellites [19]. Mounted on mobile platforms, a bistatic SAR can perform HRWS sensing by making use of the relative movements between the SAR and the targets. The small-sized real antenna aperture can realize the capability of a larger aperture radar through data focusing and signal processing [20]. A clutter suppression and mobile target imaging strategy was developed in [21] for a GEO-LEO bistatic SAR system, which was robust against the quickly traveling object with the Doppler centroid ambiguity.

With a geosynchronous (GEO) SAR satellite as the transmitter, a UAV can receive the echo signals from terrestrial targets and achieve two-dimensional (2D) imaging. The flight path of the UAV receiver was planned in [22] for such a GEO-UAV bistatic SAR system to sense rough terrains. A range model was developed in [23] to address the distinctiveness of the GEO-UAV bistatic SAR echo and the variations of the orbit positions of the GEO transmitter. A motion compensation algorithm was proposed in [24] for a mini-UAV-based bistatic SAR system to address the perturbation and spatial variance of the platform. However, none of the existing works [14]–[24] have considered the BS-UAV bistatic SAR, as considered in this paper. None of the existing studies have considered the energy consumption of a UAV-based bistatic SAR system. The works in [22]–[24] were focused on data focusing or image processing algorithms, where the geosynchronous satellites transmitted dedicated signals for ground object detection and did not transmit any data. The energy consumption of the UAV was not considered in [22] for trajectory planning, and the UAV trajectory design was not addressed in [23] and [24]. The results of [22]–[24] cannot apply directly to a BS-UAV bistatic SAR system for energy-efficient trajectory design.

B. Contribution and Organization

In this paper, we propose a novel framework for cellular-aided radar sensing with a cellular-connected UAV, i.e., BS-UAV bistatic SAR sensing, where the wireless transmissions of a BS serve as the excitation signals of a bistatic SAR system, and the UAV collects the echoed signals for radar sensing. Given a series of landmarks to be sensed/observed, the UAV's trajectory is optimized to minimize its propulsion energy while satisfying the range and azimuth resolutions of sensing, thereby delivering energy-efficient BS-UAV bistatic SAR sensing missions and extending mission durations. This trajectory planning problem is non-convex because of the non-convexity of its objective function and constraints. We convexify the problem and obtain a quality solution efficiently by utilizing successive convex approximation (SCA) and block coordinate descent (BCD).

The key contributions of the paper are listed as follows.

- A novel BS-UAV bistatic SAR platform is proposed to reuse cellular downlink signals as excitation signals. A cellular-connected UAV receives the reflected signals and conducts radar sensing on landmarks.
- The range and azimuth resolutions of the BS-UAV bistatic SAR are analyzed. An effective sensing area of the BS-UAV bistatic SAR is established to effectively capture a landmark.
- The UAV's trajectory is optimized to minimize its propulsion energy and ensure that all landmarks are captured in the effective sensing areas with the required range and azimuth sensing resolutions. By applying the SCA and BCD methods, a new algorithm is developed to deliver energy-efficient trajectories with a polynomial complexity.

Extensive simulations corroborate that, in terms of energy efficiency and energy usage fluctuations, the proposed trajectory planning algorithm outperforms a baseline scheme that minimizes the flight distance of the UAV on the cellular-aided radar sensing mission. The proposed algorithm can save up to 55% of the UAV's propulsion energy, as compared to the baseline scheme.

The remainder of this paper is arranged as follows. Section II describes the system model. Section III formulates the UAV trajectory design problem for the BS-UAV bistatic SAR, and elaborates on the proposed trajectory planning algorithm. Performance evaluations are conducted in Section IV, followed by concluding remarks in Section V.

II. System Model

In the considered system, a BS is deployed to deliver downlink wireless services to cellular users. A cellular-connected UAV equipped with a side-looking SAR (receiver) flies and collects the echoes (or reflections) of the communication signals originated from the BS, to sense (metallic) objects and gain situational awareness; see Fig. 1. The signals are buffered at the UAV, and offloaded and post-processed (at the BS) after the sensing mission. Given the knowledge of the communication signals, the direct path from the BS to the UAV can be canceled. The remaining echo signals can be used to
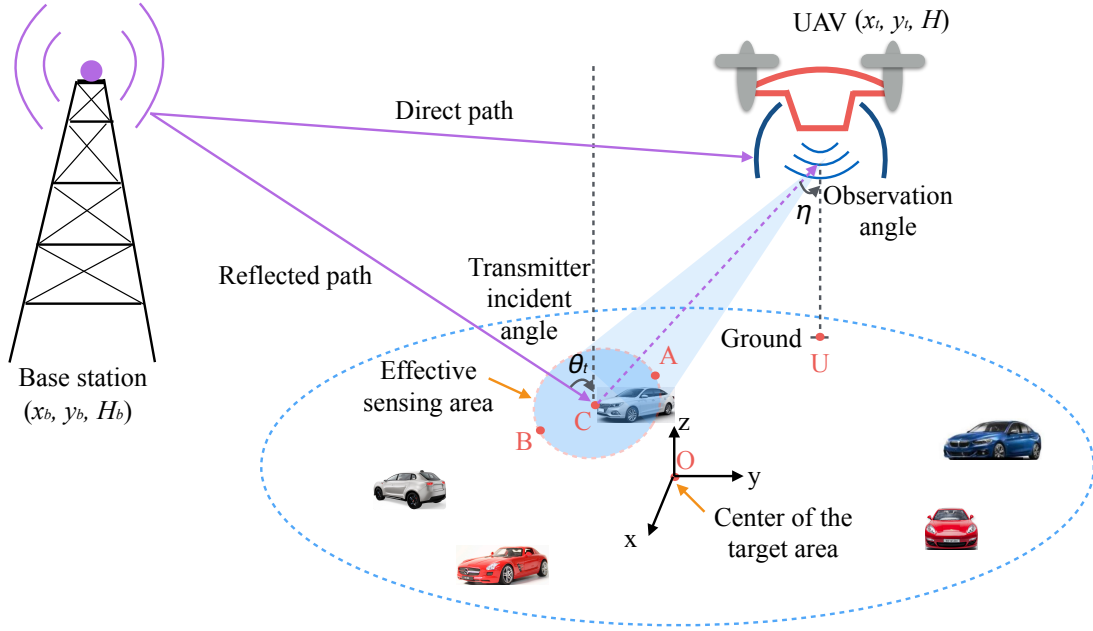
Fig. 1. System model of joint communication and radar sensing by a BS-UAV bistatic SAR, where the UAV receives the downlink cellular signals from the BS and the reflections of the signals reflected by (metalic) objects. The reflection signals can be extracted and used to produce radio/radar images and detect the objects.

sense and decide the number and locations of the objects. In this way, the UAV can perform the sensing task by utilizing the communication signals, without the need of dedicated sensing signals, and thereby reduces the radio fingerprint and carbon emission.

The proposed UAV-based sensing platform is insusceptible to inter-cell interference, since it does not need to detect or decode data signals. The transmissions from other BSs can serve as additional illuminating sources to enhance the reflection on the objects. The UAV may utilize the pilot signals of the BSs to extract the reflections of objects [25]. With the knowledge of the pilot signals, the collected reflection signals by the UAV can be correlated to cancel the direct paths from any BSs and extract the reflections by the objects to detect the objects. Alternatively, the UAV may store the captured signals, and only start to process the signals after it returns from the mission and has access to the transmitted signals of the BSs. Then, correlation can be conducted between the captured signals and the transmitted signals to extract the reflections and detect the objects. On the other hand, the proposed trajectory planning algorithm can be performed at the UAV with limited assistance of the BSs. It only requires the information of the landmarks prior to the trajectory planning. The inter-cell interference has little impact on the algorithm, when the algorithm is in operation.

A. Object Distribution

Consider a 2D ground region $\mathcal{A}$ with radius R. We assume that $\mathcal{A}$ is inside the coverage area of the BS. The number of illuminating (e.g., metallic) objects in $\mathcal{A}$, denoted by $N(\mathcal{A})$, follows the homogeneous spatial Poisson point process (SPPP). The reason is that the points are uniformly distributed

in the circular area (with the same density λ). The probability density function (PDF) is given by [26]

$$\Pr(N(\mathcal{A}) = n) = \frac{\lambda|\mathcal{A}|^n}{n!} e^{-\lambda|\mathcal{A}|}, n = 0, 1, \ldots, \quad (1)$$

where $\lambda > 0$ is the intensity, and $|\mathcal{A}|$ is the Lebesgue measure for the size of the region. The objects are uniformly randomly distributed in $\mathcal{A}$.

Let d_i, $i = 1, \cdots, N(\mathcal{A})-1$, collect the Euclidean distances from an arbitrarily selected (and designated) object to the other $(N(\mathcal{A})-1)$ objects within the disk region with radius R; and assume that d_i, $i = 1, \cdots, N(\mathcal{A})-1$, are independent and identically distributed (i.i.d.), non-negative random variables. Given the uniform stationary distribution of the objects in the disk region with radius R, the cumulative density function (CDF) of d_i, $i = 1, \cdots, N(\mathcal{A})-1$ is given by [27][1]

$$\begin{aligned} F_{d_i}(l) = 1 + \frac{2}{\pi}\left(\frac{l^2}{R^2} - 1\right)\cos^{-1}\left(\frac{l}{2R}\right) \\ - \frac{1}{\pi R}\left(1 + \frac{l^2}{2R^2}\right)\sqrt{1 - \frac{l^2}{4R^2}}, \ 0 \le l \le 2R. \end{aligned} \quad (2)$$

Let $d_{\min}$ denote the shortest of the distance between two objects, i.e., $d_{\min} = \min_{i=1,\cdots,N-1}\{d_i\}$. By exploiting Order

---

[1]Given the uniform stationary distribution of the objects in the disk region with radius R, the PDF of d_i, $i = 1, \cdots, N(\mathcal{A})-1$ is given by [27]

$$f_{d_i}(l) = \frac{2l}{R^2}\left(\frac{2}{\pi}\cos^{-1}\left(\frac{l}{2R}\right) - \frac{l}{\pi R}\sqrt{1 - \frac{l^2}{4R^2}}\right), 0 \le l \le 2R.$$

Statistics, the CDF of $d_{\min}$ can be given by

$$
\begin{aligned}
F_{d_{\min}}(l) &= 1 - [1 - F_{d_i}(l)]^{N(\mathcal{A})-1} \\
&= 1 - \left[\frac{1}{\pi R}\left(1 + \frac{l^2}{2R^2}\right)\sqrt{1 - \frac{l^2}{4R^2}} \right. \\
&\qquad\quad \left. - \frac{2}{\pi}\left(\frac{l^2}{R^2} - 1\right)\cos^{-1}\left(\frac{l}{2R}\right) \right]^{N(\mathcal{A})-1}.
\end{aligned} \tag{3}
$$

The resolution of the proposed UAV-based bistatic SAR platform is set to be finer than the expected shortest distance between two neighboring objects, i.e., $d_{\min}$, to reasonably distinguish any two different objects. For this reason, we derive the expectation of $d_{\min}$ based on the CDF in (3). The expectation is an integral over l, the distance between any two objects in the circular coverage area of the BS with the radius of R. Here, $0 \le l \le 2R$. Then, the expectation of $d_{\min}$ can be given by

$$
\begin{aligned}
\mathbb{E}\left[d_{\min}\right] &= \int_0^{2R} l\, dF_{d_{\min}}(l) \\
&= -l\left[-F_{d_i}(l)\right]^{N(\mathcal{A})-1}\Big|_0^{2R} + \int_0^{2R}\left[1 - F_{d_i}(l)\right]^{N(\mathcal{A})-1} dl \\
&= \int_0^{2R}\left[\frac{1}{\pi R}\left(1 + \frac{l^2}{2R^2}\right)\sqrt{1 - \frac{l^2}{4R^2}}\right. \\
&\qquad\quad \left. - \frac{2}{\pi}\left(\frac{l^2}{R^2} - 1\right)\cos^{-1}\left(\frac{l}{2R}\right)\right]^{N(\mathcal{A})-1} dl,
\end{aligned} \tag{4}
$$

where $F_{d_i}(0) = 1 - \frac{1}{\pi R}$ and $F_{d_i}(2R) = 1$.

B. UAV Mobility

In practice, the receiver of a bistatic SAR system flies at a constant altitude, as a stable flight can stabilize the accuracy of the SAR [28]. For this reason, we consider a horizontally flying UAV at a constant altitude, H (in meters), in line with practical implementations, and focus this paper on 2D trajectory planning. Nevertheless, the algorithm developed in this paper can be potentially extended to three-dimensional (3D) trajectory planning with varying UAV altitudes $H_t, \forall t$, as will be discussed in Section III.

The UAV executes the sensing mission for a fixed time horizon of T seconds, which is divided into T_w time slots indexed by t, and $t = 1, \ldots, T_w$. The duration of a time slot t is δ seconds. The UAV's time-varying 2D coordinates are $\mathbf{q}_t = [x_t, y_t]^T, \forall t$, with the initial location $\mathbf{q}_0 = [x_0, y_0]^T$. Let V_t denote the UAV speed at time slot t, which is upper bounded by V_m. The UAV's mobility constraint is given by

$$
\|\mathbf{q}_t - \mathbf{q}_{t-1}\| = \delta V_t \le \delta V_m, \ \forall t. \tag{5}
$$

For a rotary-wing UAV at a speed V_t, the propulsion power at time slot t, denoted by P_t, is shown by [10]

$$
\begin{aligned}
P_t = P_0\left(1 + \frac{3V_t^2}{U_{tip}^2}\right) + P_1\left(\sqrt{1 + \frac{V_t^4}{4v_0^4}} - \frac{V_t^2}{2v_0^2}\right)^{\frac{1}{2}} \\
+ \frac{1}{2}d_f s \rho A V_t^3,
\end{aligned} \tag{6}
$$

where P_0 and P_1 stand for the fixed *blade* and *induced powers* when the aircraft hovers, respectively; U_{tip} denotes the rotor velocity; v_0 is the mean rotor velocity when the aircraft hovers; d_f and s stand for the fuselage drag fraction and rotor solidity, respectively; and ρ and A are the gaseous density and rotor disc area, respectively.

C. Airborne Bistatic Side-Looking SAR

As shown in Fig. 1, the effective sampling SAR sensing area of the UAV, denoted by $\mathcal{U}_t$, is an ellipsoid centered at point C as per slot t. We assume that the effective sensing area $\mathcal{U}_t$ is always to the right of the UAV, by considering a side-looking SAR [29]. The major axis of the ellipsoid $\mathcal{U}_t$, L_{AB}, is perpendicular to the UAV's heading. Let $\alpha_t \in [0, 2\pi)$ denote the angle between the UAV's heading and the x-axis at time slot t. We have

$$
\sin\alpha_t = \frac{y_t - y_{t-1}}{\delta V_t}; \quad \cos\alpha_t = \frac{x_t - x_{t-1}}{\delta V_t}. \tag{7}
$$

Further let $\eta \in (0, \pi/2)$ denote the observation angle of the side-looking SAR at the UAV, which is fixed over time. Given the horizontal coordinates of the UAV, i.e., $U = (x_t, y_t)$ at slot t, and $L_{UC} = H\tan\eta$, the coordinates of the center C, i.e., $\mathbf{q}_c^t = [x_c^t, y_c^t]^T$, can be written as

$$
x_c^t = x_t + H\tan\eta\sin\alpha_t; \quad y_c^t = y_t - H\tan\eta\cos\alpha_t. \tag{8}
$$

To guarantee the sensing performance, C should always be inside the target area $\mathcal{A}$. We have $L_{OC} \le R, \ \forall t$.

At any time slot t, the range resolution δ_r^t and the azimuth resolution δ_a^t of the BS-UAV bistatic SAR are given by [29, Eq. (5)], [30, Eqs. (24) & (29)]

$$
\delta_r^t = \frac{c}{B(\sin\eta + \sin\theta_t)}; \tag{9a}
$$

$$
\delta_a^t = \frac{\lambda_c H}{T_d V_t \cos\eta}, \tag{9b}
$$

where c is the speed of light, λ_c is the wavelength, B is the transmit signal bandwidth of the BS, $\theta_t \in (0, \pi/2)$ is the incidence angle of the transmitted signal (from the BS) with respect to the point C, and T_d is the coherent SAR integration time [31]. Given the horizontal coordinates of the BS $\mathbf{q}_b = [x_b, y_b]^T$ and its height H_b, we have

$$
\sin\theta_t = \frac{\|\mathbf{q}_c^t - \mathbf{q}_b\|}{\sqrt{\|\mathbf{q}_c^t - \mathbf{q}_b\|^2 + H_b^2}}. \tag{10}
$$

In order to distinguish the objects, the resolution of the SAR has to be finer than the shortest expected distance between any two objects, $d_{\min}$, i.e., $\delta_r^t \le d_{\min}$ and $\delta_a^t \le d_{\min}$. This resolution requirement is used to detect and differentiate different objects by leveraging the typically narrow signal bandwidths of cellular systems and, in turn, the poor resolution of sensing [32]. It is worth mentioning that we do not consider object identification in this paper, as it would require wider signal bandwidths to achieve better resolutions for detecting the shape of an object or even imaging the object [30]. Nevertheless, the proposed trajectory planning algorithm would still be relevant under a wider signal bandwidth and correspondingly
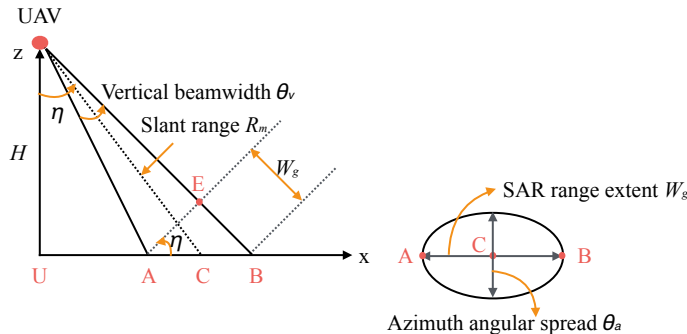
Fig. 2. The (x, z)-plane view of the side-looking BS-UAV bistatic SAR effective sensing area, where the UAV heading is perpendicular to the paper, and W_g is the SAR range extent.

a finer resolution requirement. The algorithm is generic and suitable for different resolution requirements.

Considering the characteristics of the side-looking SAR, the cosine of the UAV elevation angle is

$$\cos\eta \approx \frac{L_{\text{AE}}}{W_g} \approx \frac{\theta_v R_m}{W_g} \approx \frac{\lambda_c R_m}{W_a W_g}, \tag{11}$$

where R_m is the slant range (distance) from the SAR antenna to the center of $\mathcal{U}_t$ (i.e., point C); W_a is the height of the SAR antenna, and W_g is the SAR range extent, i.e., the width of the ground swath covered by the SAR beam, to the right of the UAV; and the vertical beamwidth of the SAR is $\theta_v = \lambda_c/W_a$. The azimuth angular spread is $\theta_a = \lambda_c/L_a$, with L_a being the antenna length parallel to the direction of the UAV's heading. This spread is due to the interference of the waves emitted from and received by the dipoles of the antenna [33].

The effective sensing area is ellipsoidal, denoted by $\mathcal{U}_t$. The ellipsoidal effective sensing area is significantly smaller than the coverage area of the BS, $\mathcal{A}$, and is used to sample different parts of the coverage area for object detection. The major and minor axes of the ellipsoidal sensing area, $\mathcal{U}_t$, are $W_g = \frac{\lambda_c R_m}{W_a \cos\eta}$ and $\theta_a = \lambda_c/L_a$, respectively. We can obtain from Fig. 2 that $R_m = H/\cos\eta$. Therefore, at any moment, the size of the effective sensing area $\mathcal{U}_t$, i.e., S, is

$$S = \frac{\pi}{4} \times \frac{\lambda_c}{L_a} \times \frac{\lambda_c H}{W_a \cos^2\eta}. \tag{12}$$

Given the range and azimuth resolutions of the SAR, and the center and size of the effective sensing area, the BS-UAV bistatic SAR can efficiently sense, detect, and distinguish ground objects in the disk region while the UAV is flying. The details are provided in Section III.

III. Proposed Framework for UAV-assisted Joint Communication and Radar Sensing

The UAV performs sensing at a series of landmarks at specified time. The BS-UAV bistatic SAR satisfies the resolution requirements to distinguish objects. The 2D coordinates of the landmark to be sensed at the t-th time slot are $\mathbf{q}_g^t = [x_g^t, y_g^t]^T$, $\forall t$. We have $G \in \mathcal{U}_t$, $\forall t$.

Through antenna configuration, the ellipsoidal shape of $\mathcal{U}_t$ can be approximated by a circular area, i.e., $\theta_a = W_g$. The

landmark of interest is inside the sensing area $\mathcal{U}_t$. Therefore, the distance between the landmark G and the center of the sensing area $\mathcal{U}_t$, i.e., point C, must not exceed the radius of $\mathcal{U}_t$ at any time slot t. With the coordinates of the center C and the diameter of $\mathcal{U}_t$, i.e., λ_c/L_a, we have

$$\|\mathbf{q}_g^t - \mathbf{q}_c^t\| \leq \frac{\lambda_c}{2L_a}, \ \forall t. \tag{13}$$

The UAV flies at a constant altitude H, and detects objects. The UAV minimizes the overall propulsion energy consumption during the considered time horizon, while maintaining acceptable sensing resolution by reusing cellular communication signals. This can be formulated as

$$\min_{\{\mathbf{q}_t, V_t, \forall t\}} \sum_{t=1}^{T_w} P_t \delta \tag{14a}$$

$$\text{s.t.} \ \frac{c}{B(\sin\eta + \sin\theta_t)} \leq d_{\min}, \ \forall t, \tag{14b}$$

$$\frac{\lambda_c H}{T_d V_t \cos\eta} \leq d_{\min}, \ \forall t, \tag{14c}$$

$$\|\mathbf{q}_t - \mathbf{q}_{t-1}\| \leq \delta V_t, \ \forall t, \tag{14d}$$

$$0 \leq V_t \leq V_m, \ \forall t, \tag{14e}$$

$$\|\mathbf{q}_g^t - \mathbf{q}_c^t\| \leq \frac{\lambda_c}{2L_a}, \ \forall t, \tag{14f}$$

where constraints (14b) and (14c) are the range and azimuth resolution requirements, respectively; (14d) and (14e) are the constraints on the UAV's mobility and maximum speed, respectively; and (14f) guarantees that the landmarks of interest are always captured at given time slots.

Problem (14) is non-convex because of the non-convexity of the objective (14a) and constraints (14b) and (14f). In what follows, we employ the SCA and BCD techniques to convexify (14), and attain a quality trajectory.

A. SCA-based Convexification

The convexification starts with the non-convex term of P_t in the objective (14a), i.e., $\left(\sqrt{1 + \frac{V_t^4}{4v_0^4}} - \frac{V_t^2}{2v_0^2}\right)^{\frac{1}{2}}$ in (6), by introducing new auxiliary variables $\{q_t \geq 0, \ \forall t = 1, \cdots, T_w\}$:

$$q_t^2 = \sqrt{1 + \frac{V_t^4}{4v_0^4}} - \frac{V_t^2}{2v_0^2}, \ \forall t, \tag{15}$$

which can be reorganized as

$$\frac{1}{q_t^2} = q_t^2 + \frac{V_t^2}{v_0^2}, \ \forall t. \tag{16}$$

Herein, the second component on the right-hand side (RHS) of (6) can be replaced by a linear element $P_1 q_t$, with a newly added constraint (16). As such, P_t is transformed into

$$\tilde{P}_t := P_0 + \frac{3P_0}{U_{tip}^2} V_t^2 + P_1 q_t + \frac{d_f}{2}\rho s A V_t^3, \ \forall t. \tag{17}$$

Here, $\tilde{P}_t$ is jointly convex in (V_t, q_t).

With a fixed δ, problem (14) becomes

$$\min_{\{\mathbf{q}_t, V_t, q_t, \forall t\}} \sum_{t=1}^{T_w} \tilde{P}_t \tag{18a}$$

$$\text{s.t. } \frac{1}{q_t^2} \le q_t^2 + \frac{V_t^2}{v_0^2}, \ \forall t, \tag{18b}$$

$$(14b) - (14f).$$

Constraint (18b) is attained by slackening the equality in (16) with inequality. Problems (14) and (18) are equivalent. The reason is that, if (18b) holds with inequality for any t, one could always diminish the value of the relevant variable q_t to save the overall power until (18b) takes equality [10].

Problem (18) is still non-convex due to the non-convex constraint (18b), and nevertheless can be resolved with the SCA approach [34] through determining the global lower limit of (18b) at a specified local point. Specifically, the left-hand side (LHS) of (18b) exhibits convexity in q_t, and the RHS exhibits convexity in $\{q_t, V_t\}$. Because the first-order Taylor expansion acts as a global lower limit of a convex function [35], we can attain the lower limit for the RHS of (18b), as given by:

$$q_t^2 + \frac{V_t^2}{v_0^2} \ge q_t^{(\ell)2} + \frac{1}{v_0^2}V_t^{(\ell)2} + 2q_t^{(\ell)}\left(q_t - q_t^{(\ell)}\right) \\ + \frac{2}{v_0^2}V_t^{(\ell)}\left(V_t - V_t^{(\ell)}\right), \tag{19}$$

where $q_t^{(\ell)}$ and $V_t^{(\ell)}$ are the respective values of the variables at the ℓ-th iteration of the SCA method.

We proceed to convexify constraints (14b) and (14f), since the other constraints (14c)-(14e) are all convex by now. This starts by rewriting (14b) as

$$\sin \theta_t \ge \frac{c}{Bd_{\min}} - \sin \eta. \tag{20}$$

With $\sin^2 \theta_t = 1 - \cos^2 \theta_t$, we have

$$\frac{H_b^2}{\|\mathbf{q}_c^t - \mathbf{q}_b\|^2 + H_b^2} \le 1 - \left(\frac{c}{Bd_{\min}} - \sin \eta\right)^2. \tag{21}$$

Introduce slack variables $w_t = \sin \alpha_t$ and $u_t = \cos \alpha_t, \forall t$. From (5) and (7), we have additional constraints on w_t and u_t:

$$-1 \le w_t \le \frac{y_t - y_{t-1}}{\delta V_t}, \ \forall t, \tag{22a}$$

$$\frac{x_t - x_{t-1}}{\delta V_t} \le u_t \le 1, \ \forall t. \tag{22b}$$

Constraint (22) is non-convex because of the coupling between V_t and w_t (or u_t).

With w_t and u_t, (21) can be reorganized as

$$(x_t + w_t H \tan \eta - x_b)^2 + (y_t - u_t H \tan \eta - y_b)^2 \\ \ge \frac{H_b^2}{1 - \left(\frac{c}{Bd_{\min}} - \sin \eta\right)^2} - H_b^2 := C_r, \ \forall t. \tag{23}$$

The LHS of (23) is convex in $\{\mathbf{q}_t, w_t, u_t\}$. The RHS of (23) is a constant and defined as C_r for illustration convenience, given the predetermined parameters H_b, c, B, $d_{\min}$, and η. We convexify (23) by determining the first-order Taylor expansion of its LHS at the local point attained during the ℓ-th iteration of the SCA:

Given $\{w_t^{(\ell)}, u_t^{(\ell)}\}$, (23) can be linearized in $\mathbf{q}_t$:

$$(x_t^{(\ell)} + w_t^{(\ell)} H \tan \eta - x_b)^2 + (y_t^{(\ell)} - u_t^{(\ell)} H \tan \eta - y_b)^2 \\ + 2(x_t^{(\ell)} + w_t^{(\ell)} H \tan \eta - x_b)(x_t - x_t^{(\ell)}) \\ + 2(y_t^{(\ell)} - u_t^{(\ell)} H \tan \eta - y_b)(y_t - y_t^{(\ell)}) \ge C_r, \ \forall t. \tag{24}$$

Given $\{\mathbf{q}_t^{(\ell)}, V_t^{(\ell)}, q_t^{(\ell)}\}$, (23) can be linearized in $\{w_t, u_t\}$:

$$(x_t^{(\ell)} + w_t^{(\ell)} H \tan \eta - x_b)^2 + (y_t^{(\ell)} - u_t^{(\ell)} H \tan \eta - y_b)^2 \\ + H \tan \eta(x_t^{(\ell)} + w_t^{(\ell)} H \tan \eta - x_b)(w_t - w_t^{(\ell)}) \\ + H \tan \eta(y_t^{(\ell)} - u_t^{(\ell)} H \tan \eta - y_b)(u_t - u_t^{(\ell)}) \ge C_r, \forall t. \tag{25}$$

As done to (23), constraint (14f) can be rewritten as

$$(x_t + w_t H \tan \eta - x_g^t)^2 + (y_t - u_t H \tan \eta - y_g^t)^2 \le \left(\frac{\lambda_c}{2L_a}\right)^2, \forall t, \tag{26}$$

which is convex in $\{\mathbf{q}_t, w_t, u_t\}$.

As a result, problem (18) is transformed into

$$\min_{\{\mathbf{q}_t, V_t, q_t, w_t, u_t, \forall t\}} \sum_{t=1}^{T_w} \tilde{P}_t \tag{27a}$$

$$\text{s.t. } \frac{1}{q_t^2} \le q_t^{(\ell)2} + \frac{1}{v_0^2}V_t^{(\ell)2} + 2q_t^{(\ell)}\left(q_t - q_t^{(\ell)}\right) \\ + \frac{2}{v_0^2}V_t^{(\ell)}\left(V_t - V_t^{(\ell)}\right), \ \forall t, \tag{27b}$$

$$(14c) - (14e), \ (22), \ (24) - (26).$$

where (27b) tightens the original constraint (18b) by using a lower bound of its RHS. Since problem (27) is a tightened version of problem (18), the feasible region of (27) is also the feasible region of (18); not the other way around.

B. Block Coordinate Descent (BCD)

Problem (27) is still non-convex due to the non-convexity of constraint (22). We apply the BCD to optimize $\{\mathbf{q}_t, V_t, q_t\}$ and $\{w_t, u_t\}$ in an alternating manner, because the variables V_t and $\{w_t, u_t\}$ are coupled in the non-convex constraint (22):

Given fixed $\{w_t, u_t\}$, problem (27) is reduced to the following convex problem:

$$\min_{\{\mathbf{q}_t, V_t, q_t, \forall t\}} \sum_{t=1}^{T_w} \tilde{P}_t \tag{28a}$$

$$\text{s.t. } w_t^{(\ell)} \le \frac{y_t - y_{t-1}}{\delta V_t}, \ \forall t, \tag{28b}$$

$$\frac{x_t - x_{t-1}}{\delta V_t} \le u_t^{(\ell)}, \ \forall t, \tag{28c}$$

$$(x_t + w_t^{(\ell)} H \tan \eta - x_g^t)^2 + (y_t - u_t^{(\ell)} H \tan \eta - y_g^t)^2 \\ \le \left(\frac{\lambda_c}{2L_a}\right)^2, \forall t, \tag{28d}$$

$$(14c) - (14e), \ (24), \ (27b).$$

Given fixed $\{\mathbf{q}_t, V_t, q_t\}$, problem (27) becomes a feasibility checking problem to find the values of $\{w_t, u_t\}$ that satisfy the following convex constraints:

$$\text{find } \{w_t, u_t, \forall t\} \tag{29a}$$

Algorithm 1 The proposed trajectory planning algorithm for the cellular-aided radar sensing to problem (14).

1: **Initialization:** Generate a feasible initial flight path for the UAV, i.e., $\{\mathbf{q}_t^{(0)}, V_t^{(0)}, q_t^{(0)}, t = 1, \cdots, T_w\}$, and input initial values for the slack variables $\{w_t^{(0)}, u_t^{(0)}, t = 1, \cdots, T_w\}$.

2: **for** $\ell = 1, 2, ...$ **do**

3: Approximate the propulsion power P_t by (17), (18b), and (19) by the SCA technique.

4: Introduce slack variables w_t and $u_t, \forall t$, and bound them by constraint (22).

5: Convexify constraint (14b) by (24) and (25), and rewrite constraint (14f) into a convex one (26).

6: Given fixed $\{w_t^{(\ell-1)}, u_t^{(\ell-1)}\}$, solve problem (28) by the interior point method to update the optimization variables $\{\mathbf{q}_t^{(\ell)}, V_t^{(\ell)}, q_t^{(\ell)}\}$ to design the UAV trajectory.

7: Given $\{\mathbf{q}_t^{(\ell)}, V_t^{(\ell)}, q_t^{(\ell)}\}$, solve problem (29) by the interior point method to update the slack variables $\{w_t^{(\ell-1)}, u_t^{(\ell-1)}\}$.

8: Update $\ell \leftarrow \ell + 1$.

9: **end for**

$$\text{s.t.} \ -1 \le w_t \le \frac{y_t^{(\ell)} - y_{t-1}^{(\ell)}}{\delta V_t^{(\ell)}}, \ \forall t, \tag{29b}$$

$$\frac{x_t^{(\ell)} - x_{t-1}^{(\ell)}}{\delta V_t^{(\ell)}} \le u_t \le 1, \ \forall t, \tag{29c}$$

$$(x_t^{(\ell)} + w_t H \tan\eta - x_g^t)^2 + (y_t^{(\ell)} - u_t H \tan\eta - y_g^t)^2$$
$$\le \left(\frac{\lambda_c}{2L_a}\right)^2, \ \forall t, \tag{29d}$$

$$(25).$$

Problems (28) and (29) can be solved by existing convex tools, such as MATLAB CVX.

When considering 3D trajectory planning, we can potentially decouple the optimizations of the 2D horizontal trajectory and the altitude by using alternating optimization techniques. Given fixed altitudes of the UAV $H_t, \forall t$, the 2D trajectory can be designed using the proposed Algorithm 1. Given fixed 2D trajectory (and auxiliary variables), i.e., $\{\mathbf{q}_t, V_t, q_t, w_t, u_t, \forall t\}$, the varying UAV altitude $H_t, \forall t$, can be potentially optimized by solving a similar subproblem to (29) by replacing w_t and u_t with H_t in (29a), and H with H_t in (29d). The subproblem can be convexified and solved in the same way as problem (29), as described in Algorithm 1. The horizontal trajectory and the altitude can be optimized in an alternating manner until convergence. The detailed design and validation of the 3D trajectory planning will be presented in our subsequent study.

C. Algorithm and Complexity

Algorithm 1 summarizes the steps proposed in this section to convexify and solve efficiently problem (14). The algorithm is computationally dominated by Steps 6 and 7, as Steps 3 to 5 compute linear functions with a complexity of $\mathcal{O}(N)$. After a series of mathematical manipulations and transformations,

TABLE I
THE PARAMETERS OF THE BS-UAV BISTATIC SAR [10], [30]

Parameter	Value
Transmission bandwidth, B	150 MHz
Wavelength, λ_c	0.1 m
Coherent integration time, T_d	1 s
SAR observation angle, η	$\pi/4$
Minimum object distance, $d_{\min}$	20 m
UAV weight and altitude, H	2 kg, 1000 m
Maximum UAV speed, V_m	50 m/s
Blade profile power and tip speed, P_0 and U_{tip}	3.4 W, 60 m/s
Rotor induced power and velocity, P_1 and v_0	118 W, 5.4 m/s
Rotor solidity and disc area, s and A	0.02, 0.5 m^2
Air density and fuselage drag fraction, ρ and d_f	1.225 kg/m^3, 0.3

the original problem (14) is recast as (27) with a convex objective and non-convex constraints, and further decomposed into two subproblems, i.e., problems (28) and (29), to convexify the non-convex constraints. Problems (28) and (29) are convex programs, given their convex objective functions and constraints (i.e., all the constraints are either linear or quadratic). In this sense, Steps 6 and 7 each solve a convex program and update the optimization variables, i.e., by running the interior point method with the complexity of $\mathcal{O}(N^{3.5})$ per iteration [36]. The overall computational complexity of Algorithm 1 is $\mathcal{O}(N^{3.5})$ per iteration. Interested readers can refer to [35] for a detailed introduction of the interior point method and convex optimization in general.

Let $\mathbf{x}$ and $\mathbf{x}^*$ denote a feasible solution and the optimal solution to problem (27), respectively. Also, let P denote the objective value of problem (27). As established in [37], given the convergence precision ϵ of the algorithm, i.e., $|P(\mathbf{x}) - P(\mathbf{x}^*)| \le \epsilon$, the interior-point method takes $\mathcal{O}(\log\frac{1}{\epsilon})$ iterations before convergence. Therefore, Algorithm 1 has a polynomial complexity of $\mathcal{O}(N^{3.5}\log\frac{1}{\epsilon})$.

IV. SIMULATION RESULTS

This section provides the simulation results of the proposed trajectory planning algorithm for BS-UAV bistatic SAR using MATLAB. The entire sensing period lasts $T = 300$ s with each time slot of $\delta = 0.5$ s, unless stated otherwise. The default setting of the landmarks (and associated sensing time) is a series of points with the first 15 of them, i.e., when $t \le 150$ s, along the y-axis starting from $(0, 0)$, and the rest along the x-axis starting from $\mathbf{q}_g^{16}$. The adjacent landmarks are apart for an equal distance. The UAV initial location is $\mathbf{q}_0 = [-1000, -500]^T$ m. The BS is located at $\mathbf{q}_b = [1000, -1000]^T$ m, with the height $H_b = 50$ m. The other parameters concerning the BS-UAV bistatic SAR sensing performance and the UAV propulsion power are provided in Table I.

We note that the standard sub-6 GHz band has been extensively deployed to provide broad 5G coverage, where the antennas are typically horizontally or quasi-horizontally oriented in the sub-6 GHz band [32]. The transmission bandwidth is typically narrow in the sub-6 GHz band, e.g., up to 100 MHz,
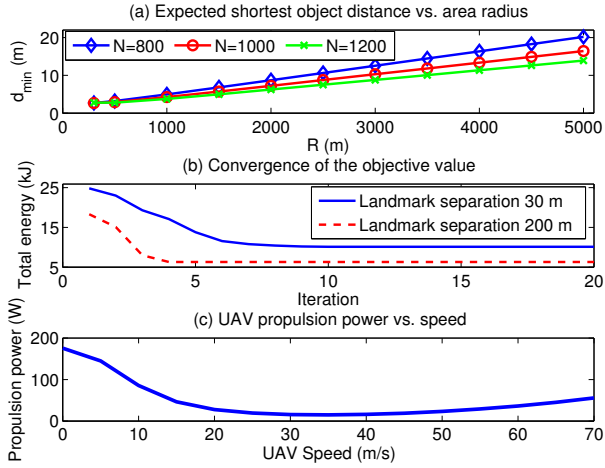
Fig. 3. Fig. 3(a) plots the expected shortest distance between any two objects in the area, $d_{\min}$, vs. the radius of the given area, R; Fig. 3(b) plots the convergence of the objective value (27a) under the default setting; and Fig. 3(c) plots the UAV propulsion power vs. speed.
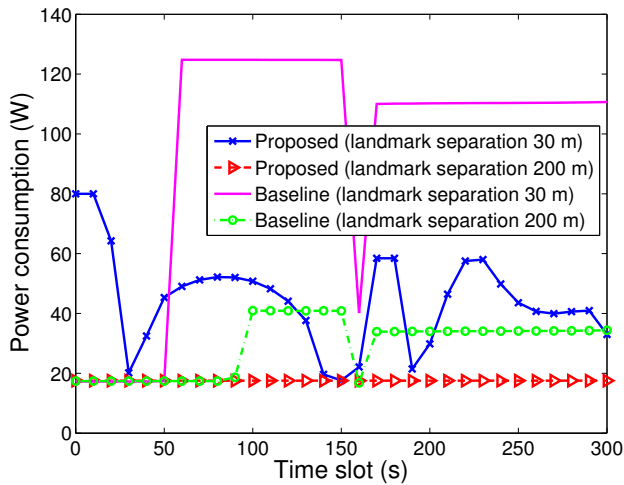

Fig. 5. The UAV trajectory by the proposed and baseline schemes, where the landmarks of interest are separated by 30 m, and $H = 1000$ m.

Fig. 4. The UAV per-slot energy consumption by the proposed and baseline schemes when the landmarks of interest are separated by 30 m and 200 m, under the default setting.

Fig. 6. The UAV trajectory by the proposed and baseline schemes, where the landmarks of interest are separated by 200 m, and $H = 1000$ m.

and consequently the range resolution could be poor [38]. Nevertheless, a bandwidth of 150 MHz can be achieved in a standard sub-6 GHz band by using carrier aggregation techniques [39]. For instance, China Mobile deployed a 4G and 5G concurrent integrated network supporting a transmission bandwidth of up to 160 MHz at the 2.6 GHz band in 2019 [40]. On the other hand, the 5G new radio (NR) has also specified the use of mmWave bands. The propagation of mmWave signals can be limited within a close range of the BS, subject to antenna orientation (i.e., downtilt) [32]. Nevertheless, the signals can still be reflected by objects (e.g., with smooth metallic surfaces) or the edges of objects [41], [42], and captured by the UAV. Given the quasi-optical property of mmWave signals [43], the ground reflections (and reflections by other non-smooth surfaces, e.g., walls, vegetation, etc.) are
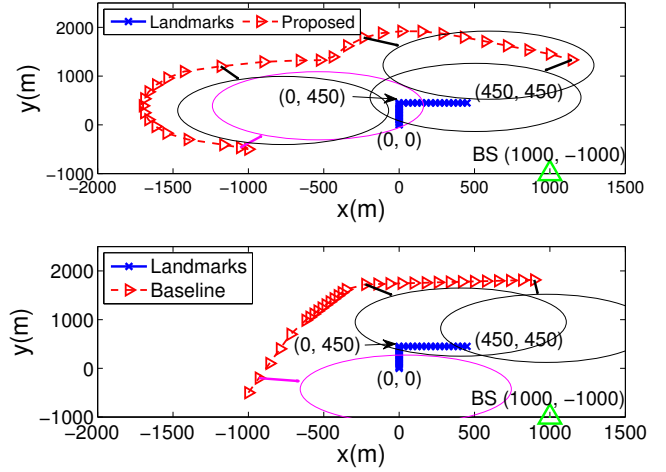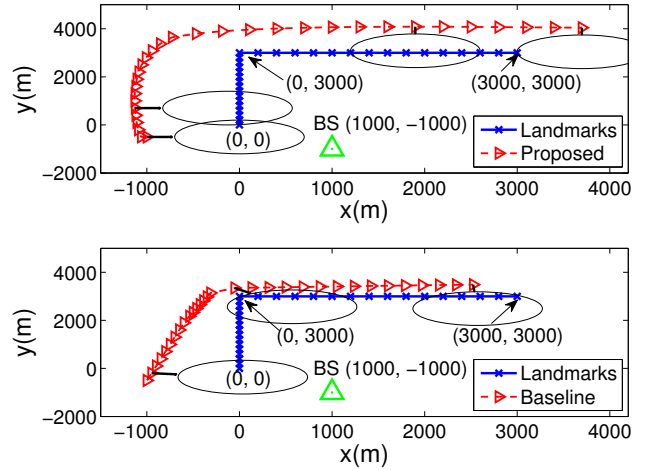
expected to be substantially weaker, resulting in strong contrast to manifest objects [43].

We also note that no existing studies have addressed the problem of energy-efficient trajectory design for the considered UAV-based bistatic SAR system, as discussed in Section I-A. In other words, no existing algorithm is directly comparable to the proposed algorithm. With due diligence, we come up with a new baseline scheme for the considered problem, which minimizes the total flight distance of the UAV without considering the energy consumption of the UAV, i.e., $\min_{\mathbf{q}_t} \sum_t \|\mathbf{q}_t\|$. The baseline has a convex objective function, while its constraints can be convexified in the same way as done in Algorithm 1.

Fig. 3(a) shows the expected shortest distance between any two objects in the area, $d_{\min}$, versus the radius of the given area $\mathcal{A}$, R (in meters), when there are $N = 800$, 1000 or 1200 objects in $\mathcal{A}$. It can be seen that $d_{\min}$ increases with R, given the number of objects in the area; i.e., the objects
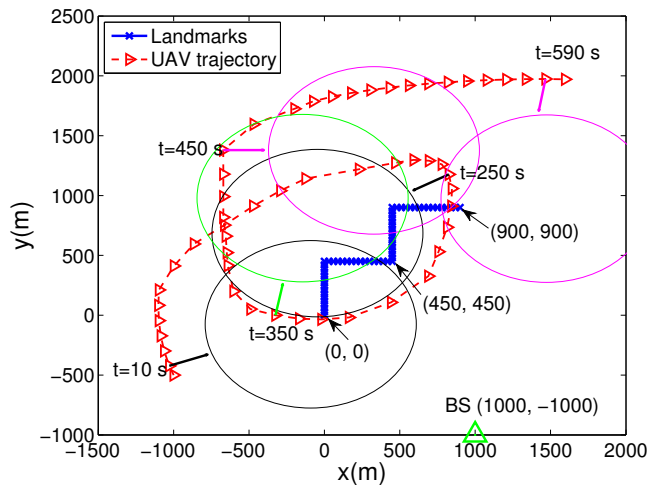
Fig. 7. The UAV trajectory by the proposed scheme, where the landmarks of interest are separated by 30 m, $H = 1000$ m, and $T = 600$ s.
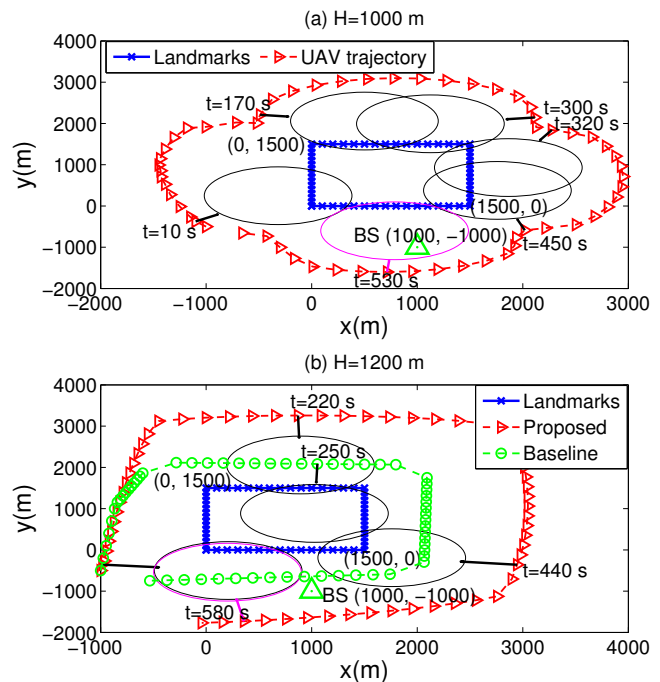

Fig. 8. The UAV trajectory by the proposed scheme, where the landmarks of interest are separated by 100 m and $T = 600$ s.
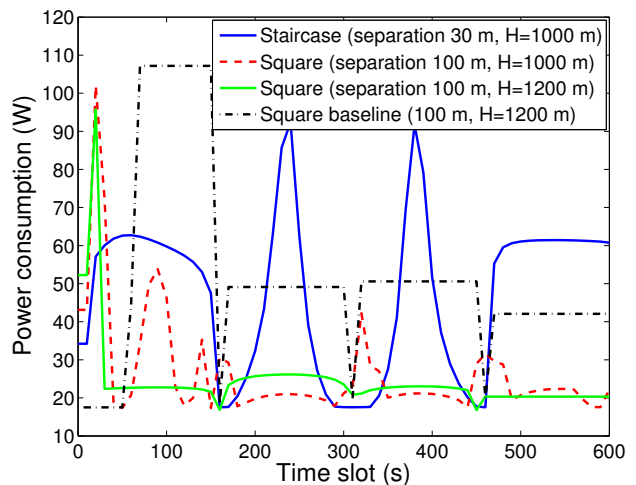

Fig. 9. The UAV per-slot energy consumption by the proposed scheme when the landmarks of interest are distributed like a staircase (separated by 30 m, $H = 1000$ m), and a square (separated by 100 m, $H = 1000$ m and 1200 m), and $T = 600$ s.

are more sparsely distributed when the area is larger. When $R = 5000$ m, the expected shortest distance between any two objects in the area $d_{\min}$ is about 20 m. Therefore, we choose the value of $d_{\min} = 20$ m. Fig. 3(b) depicts the convergence of the proposed scheme when the landmarks are separated by 30 m and 200 m under two settings. It can be seen that the objective function of problem (27), i.e., (27a), can quickly converge within about only 20 iterations. When the two neighboring landmarks are apart for a longer distance, the UAV consumes less energy and shows better energy efficiency. This is because the UAV can move faster, and the propulsion power first decreases and then increases at the increasing speed of the UAV, as shown in Fig. 3(c). Fig. 3(c) plots the UAV power consumption P_t in (6) by varying the instantaneous speed of a rotary-wing UAV from 0 m/s to 70 m/s. The UAV's propulsion power is independent of its trajectory and heading. The UAV consumes the least power when its speed is about 35 m/s, validating the results in Fig. 3(b).

Fig. 4 shows the per-slot energy consumption of the rotary-wing UAV conducting the BS-UAV bistatic SAR sensing under the proposed and baseline schemes, where the default setting of the landmarks is considered, i.e., with an equal distance of 30 m or 200 m between adjacent landmarks. It is revealed that the minimization of the flight distance does not necessarily lead to the minimization of the UAV's energy consumption. When the landmarks are separated by 30 m, the proposed scheme can save 55% of the total energy, as compared to the baseline.

It is interesting to notice that the baseline scheme is better than the proposed algorithm in terms of per-slot UAV power consumption when $t \leq 50$ s and the spacing between adjacent landmarks is 30 m. This is because the objective of the proposed algorithm, i.e., (14a), is to minimize the total energy consumption. As a result, the algorithm has the UAV fly slowly away from a landmark (while still keeping the landmark within its effective sensing area) at the beginning of the sensing mission to benefit the later stage of the mission in Fig. 4. The

UAV has to restrain its speed at the beginning of the mission at the cost of high energy consumption, as will be shown in Fig. 5. On the other hand, the baseline scheme requires the UAV to fly fast towards the landmarks in the beginning and then slows down, to minimize the total flight distance to sense all landmarks. As a result, the baseline scheme consumes less energy than the proposed algorithm at the beginning of the mission. Nevertheless, the proposed algorithm is much more energy-efficient when the entire mission is considered.
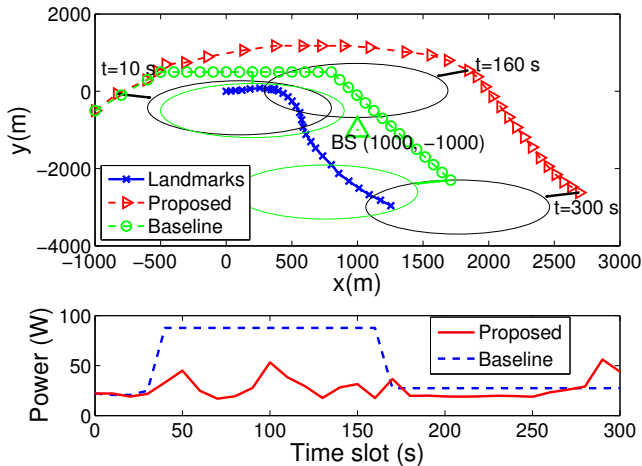
Fig. 10. The UAV trajectory and per-slot energy consumption by the proposed and baseline schemes when the landmarks of interest are distributed randomly, $H = 1000$ m and $T = 300$ s.
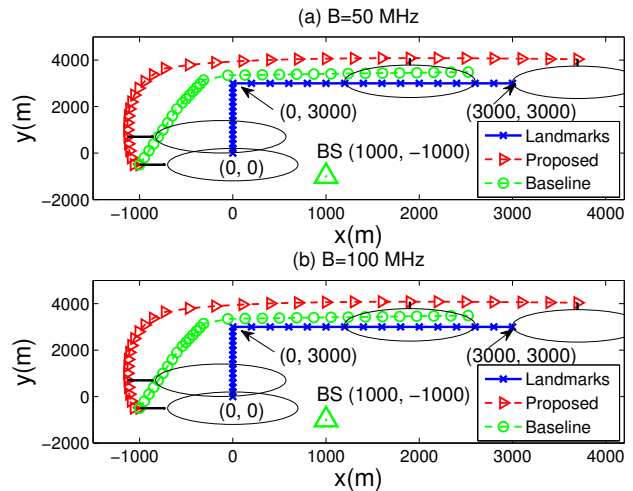

Fig. 11. The UAV trajectory by the proposed and baseline schemes when the landmarks of interest are separated by 200 m, and the transmission bandwidth is 50 MHz and 100 MHz under the default setting.

TABLE II
THE RANGE RESOLUTIONS OF THE BS-UAV BISTATIC SAR UNDER DIFFERENT TRANSMISSION BANDWIDTHS, WHERE THE TRANSMITTER INCIDENT ANGLE IS $\theta_t = \pi/3$

Transmission bandwidth, B (MHz)	50	100	150	200
Range resolution, δ_r (m)	3.81	1.91	1.27	0.95

Figs. 5 and 6 plot the UAV trajectory (the red dash line with triangle markers) and its sensing performance under the proposed and baseline schemes. The black and magenta circles provide some examples of the effective sensing areas at different time slots. The green triangle shows the location of the BS. We see in Figs. 5 and 6 that the UAV can always capture the landmarks within its sensing area at the time slots required. Under the proposed schemes, the UAV seeks an energy-efficient flight path, and is better adapted to the distribution of the landmarks. In contrast, under the baseline schemes, the UAV first catches up with the nearest landmark at its highest speed, and then flies at a relatively stable speed to satisfy the resolution requirements. This can cause drastic changes in the instantaneous power consumption of the UAV under the baseline method, as already shown in Fig. 4.

Fig. 7 plots the UAV trajectory when $T = 600$ s. The landmarks are separated by 30 m and distributed in a staircase (that is, two street blocks situated along a diagonal). The effective sensing area of the BS-UAV bistatic SAR is indicated by the black, magenta, or green circles, when $t = 10$ s, 250 s, 350 s, 450 s, and 590 s, respectively. It is shown in Fig. 7 that the BS-UAV bistatic SAR can always capture the landmarks in its sensing coverage at the required time slots.

Fig. 8 plots the UAV trajectory when the landmarks are separated by 100 m and distributed in a square (e.g., a closed loop around a triangular street block), $T = 600$ s, and $H = 1000$ m (Fig. 8(a)) or 1200 m (Fig. 8(b)). The effective sensing area of the BS-UAV bistatic SAR is shown when $t = 10$ s, 170 s, 300 s, 320 s, 450 s, and 530 s, under the UAV elevation of $H = 1000$ m, and when $t = 10$ s, 220 s, 440 s, and 580 s, under the UAV elevation of $H = 1200$ m. It is observed that the UAV intends to fly around the landmarks for both effective sensing and energy saving. The UAV trajectory of the corresponding baseline scheme is shown in Fig. 8(b) when $H = 1200$ m; see the green dashed line with circle markers. The effective sensing area of the UAV is illustrated when $t = 250$ s. We see that the UAV takes a much shorter flight

path around the landmarks to satisfy the sensing resolution requirements, which is at the cost of a much higher propulsion energy consumption, as to be shown in Fig. 9.

Fig. 9 plots the per-slot energy consumption of the proposed scheme when the landmarks are distributed in a staircase (i.e., the two diagonally situated street blocks) or a square (i.e., the closed loop of a triangular street block), with the spacing of 30 m and 100 m, respectively. Here, $T = 600$ s, and $H = 1000$ m or 1200 m. We see that the UAV consumes less energy when the landmark spacing or the UAV altitude is larger, as the UAV embraces more flexibility to design an energy-efficient trajectory and meet the sensing requirements. The per-slot energy consumption of the baseline approach is also plotted for the landmarks arranged on the square with the spacing of 100 m, and the UAV elevation is $H = 1200$ m. We see that the proposed scheme consumes dramatically lower energy than the baseline, and prevents drastic fluctuations in the per-slot consumption of the UAV propulsion energy.

Fig. 10 plots the UAV trajectory and per-slot energy consumption of the proposed and baseline schemes, when the spacing between neighboring landmarks obeys a random uniform distribution within $[0, 100]$ m. The averaged results of 20 independent realizations of the landmark locations are plotted. While the UAV flies a longer distance under the proposed algorithm than it does under the baseline approach as shown in the top of the figure, the energy consumption is substantially lower and undergoes much smaller fluctuations under the proposed algorithm as shown in the bottom of the figure. This again corroborates the merits of the proposed scheme over

the baseline scheme in terms of energy efficiency and energy consumption fluctuation.

Last but not least, we examine the performance of the proposed BS-UAV bistatic SAR under different transmission bandwidths B in the sub-6 GHz band and the mmWave band. Table II shows the range resolutions of the SAR, where B is 50 MHz, 100 MHz, and 150 MHz at the sub-6 GHz band, and 200 MHz at the mmWave band. Here, θ_t is assumed to be $\pi/3$. We see that the resolutions are always better than the expected shortest distance between any two objects, $d_{\min}$; in other words, the SAR can effectively distinguish ground objects. Fig. 11 shows the UAV trajectory by the proposed and baseline schemes, where the landmarks are separated by 200 m, and the transmission bandwidth B is 50 MHz and 100 MHz. The other settings are consistent with those in Fig. 6. By comparing Fig. 11 to Fig. 6, we see that the UAV trajectory has similar patterns while satisfying the sensing accuracy.

V. CONCLUSION

This paper proposed a novel framework of cellular-aided radar sensing with a BS-UAV bistatic SAR platform. The trajectory of the UAV was optimized to minimize the propulsion energy while satisfying the range and azimuth resolutions of sensing. The trajectory planning problem was convexified and solved efficiently by utilizing the SCA and BCD methods. Extensive simulations revealed that, in terms of energy efficiency and effective consumption fluctuation, the proposed trajectory planning algorithm is superior to its alternative that minimizes the flight distance of a cellular-aided sensing mission. The energy saving can be as large as 55% for the UAV, by running the proposed algorithm. In the future, we will extend the BS-UAV bistatic SAR system to a fixed-wing UAV-based platform, where a more sophisticated propulsion energy model and dynamic/mobility model will be taken into account.

REFERENCES

[1] S. Hu, X. Chen, W. Ni, E. Hossain, and X. Wang, "Distributed machine learning for wireless communication networks: Techniques, architectures, and applications," *IEEE Commun. Surveys Tuts.*, vol. 23, no. 3, pp. 1458–1493, 3rd Quart. 2021.

[2] P. Kumari, J. Choi, N. González-Prelcic, and R. W. Heath, "IEEE 802.11ad-based radar: An approach to joint vehicular communication-radar system," *IEEE Trans. Veh. Tech.*, vol. 67, no. 4, pp. 3012–3027, Apr. 2018.

[3] J. A. Zhang, M. L. Rahman, K. Wu, X. Huang, Y. J. Guo, S. Chen, and J. Yuan, "Enabling joint communication and radar sensing in mobile networks: A survey," *IEEE Commun. Surveys Tuts.*, vol. 24, no. 1, pp. 306–345, 1st Quart. 2022.

[4] C. Sturm and W. Wiesbeck, "Waveform design and signal processing aspects for fusion of wireless communications and radar sensing," *Proc. IEEE*, vol. 99, no. 7, pp. 1236–1259, Jul. 2011.

[5] Y. Luo, J. A. Zhang, X. Huang, W. Ni, and J. Pan, "Optimization and quantization of multibeam beamforming vector for joint communication and radio sensing," *IEEE Trans. Commun.*, vol. 67, no. 9, pp. 6468–6482, Sep. 2019.

[6] L. B. Stotts, S. Karp, and J. M. Aein, "The origins of miniature global positioning system-based navigation systems [SP history]," *IEEE Signal Process. Mag.*, vol. 31, no. 6, pp. 114–117, Nov. 2014.

[7] T. E. Humphreys, M. J. Murrian, and L. Narula, "Deep-urban unaided precise global navigation satellite system vehicle positioning," *IEEE Intell. Transport. Syst. Mag.*, vol. 12, no. 3, pp. 109–122, Fall 2020.

[8] Y. Zeng, X. Xu, S. Jin, and R. Zhang, "Simultaneous navigation and radio mapping for cellular-connected uav with deep reinforcement learning," *IEEE Trans. Wireless Commun.*, vol. 20, no. 7, pp. 4205–4220, Jul. 2021.

[9] X. Yuan, Z. Feng, W. Ni, R. P. Liu, J. A. Zhang, and W. Xu, "Secrecy performance of terrestrial radio links under collaborative aerial eavesdropping," *IEEE Trans. Inf. Forensics Security*, vol. 15, pp. 604–619, Jun. 2020.

[10] Y. Zeng, J. Xu, and R. Zhang, "Energy minimization for wireless communication with rotary-wing UAV," *IEEE Trans. Wireless Commun.*, vol. 18, no. 4, pp. 2329–2345, Apr. 2019.

[11] C. Sun, W. Ni, and X. Wang, "Joint computation offloading and trajectory planning for UAV-assisted edge computing," *IEEE Trans. Wireless Commun.*, vol. 20, no. 8, pp. 5343–5358, Aug. 2021.

[12] S. Hu, Q. Wu, and X. Wang, "Energy management and trajectory optimization for UAV-enabled legitimate monitoring systems," *IEEE Trans. Wireless Commun.*, vol. 20, no. 1, pp. 142–155, Jan. 2021.

[13] S. Hu, W. Ni, X. Wang, A. Jamalipour, and D. Ta, "Joint optimization of trajectory, propulsion, and thrust powers for covert UAV-on-UAV video tracking and surveillance," *IEEE Trans. Inf. Forensics Security*, vol. 16, pp. 1959–1972, Jan. 2021.

[14] F. Liu, C. Masouros, A. Li, H. Sun, and L. Hanzo, "MU-MIMO communications with MIMO radar: From co-existence to joint transmission," *IEEE Trans. Wireless Commun.*, vol. 17, no. 4, pp. 2755–2770, Apr. 2018.

[15] F. Liu, L. Zhou, C. Masouros, A. Li, W. Luo, and A. Petropulu, "Toward dual-functional radar-communication systems: Optimal waveform design," *IEEE Trans. Signal Process.*, vol. 66, no. 16, pp. 4264–4279, Aug. 2018.

[16] J. A. Zhang, X. Huang, Y. J. Guo, J. Yuan, and R. W. Heath, "Multibeam for joint communication and radar sensing using steerable analog antenna arrays," *IEEE Trans. Veh. Tech.*, vol. 68, no. 1, pp. 671–685, Jan. 2019.

[17] Z. Ni, J. Andrew Zhang, K. Yang, X. Huang, and T. A. Tsiftsis, "Multi-metric waveform optimization for multiple-input single-output joint communication and radar sensing," *IEEE Trans. Commun.*, vol. 70, no. 2, pp. 1276–1289, Feb. 2022.

[18] I. Hajnsek and T. E. Busche, "TanDEM-X science plan," DLR Public Doc. TD-PD-PL-0069, no. 1.0, Jun. 2010.

[19] M. Bartusch, C. Bruens, A. E. Nuncio Quiroz, and S. Stettner, "HRWS: The upcoming german X-band spaceborne SAR mission," in *Proc. 13th European Conference on Synthetic Aperture Radar (EUSAR)*, Mar. 2021, pp. 1–4.

[20] W.-Q. Wang and J. Cai, "Antenna directing synchronization for bistatic synthetic aperture radar systems," *IEEE Antennas Wireless Propag. Lett.*, vol. 9, pp. 307–310, Apr. 2010.

[21] S. Zhang, Y. Gao, M. Xing, R. Guo, J. Chen, and Y. Liu, "Ground moving target indication for the geosynchronous-low earth orbit bistatic multichannel SAR system," *IEEE J. Sel. Topics Appl. Earth Observ. Remote Sens.*, vol. 14, pp. 5072–5090, May 2021.

[22] Z. Sun, J. Wu, J. Yang, Y. Huang, C. Li, and D. Li, "Path planning for GEO-UAV bistatic SAR using constrained adaptive multiobjective differential evolution," *IEEE Trans. Geosci. Remote Sens.*, vol. 54, no. 11, pp. 6444–6457, Nov. 2016.

[23] Z. Sun, J. Wu, Z. Li, H. An, and X. He, "Geosynchronous spaceborne–airborne bistatic SAR data focusing using a novel range model based on one-stationary equivalence," *IEEE Trans. Geosci. Remote Sens.*, vol. 59, no. 2, pp. 1214–1230, Feb. 2021.

[24] Z. Wang, F. Liu, T. Zeng, and C. Wang, "A novel motion compensation algorithm based on motion sensitivity analysis for mini-UAV-based BiSAR system," *IEEE Trans. Geosci. Remote Sens.*, vol. 60, pp. 1–13, Jan. 2022.

[25] A. Ghosh, A. Maeder, M. Baker, and D. Chandramouli, "5G evolution: A view on 5G cellular technology beyond 3GPP Release 15," *IEEE Access*, vol. 7, pp. 127 639–127 651, Sep. 2019.

[26] M. Haenggi, *Stochastic Geometry for Wireless Networks*. Cambridge University Press, 2012.

[27] X. Yuan, Z. Feng, W. Xu, W. Ni, J. A. Zhang, Z. Wei, and R. P. Liu, "Capacity analysis of UAV communications: Cases of random trajectories," *IEEE Trans. Veh. Tech.*, vol. 67, no. 8, pp. 7564–7576, Aug. 2018.

[28] Y. Zhang, H. Mu, Y. Jiang, C. Ding, and Y. Wang, "Moving target tracking based on improved GMPHD filter in circular SAR system," *IEEE Geosci. Remote Sens. Lett.*, vol. 16, no. 4, pp. 559–563, Apr. 2019.

[29] M. Rodriguez-Cassola, S. V. Baumgartner, G. Krieger, and A. Moreira, "Bistatic TerraSAR-X/F-SAR spaceborne–airborne SAR experiment: Description, data processing, and results," *IEEE Trans. Geosci. Remote Sens.*, vol. 48, no. 2, pp. 781–794, Feb. 2010.

[30] A. Moccia and A. Renga, "Spatial resolution of bistatic synthetic aperture radar: Impact of acquisition geometry on imaging performance,"

IEEE Trans. Geosci. Remote Sens., vol. 49, no. 10, pp. 3487–3503, Oct. 2011.

[31] F. T. Ulaby, R. K. Moore, and A. K. Fung, *Microwave Remote Sensing Active and Passive*.   Addison-Wesley, 1982, vol. II, pp. 569–572.

[32] M. Cudak, A. Ghosh, A. Ghosh, and J. Andrews, "Integrated access and backhaul: A key enabler for 5G millimeter-wave deployments," *IEEE Commun. Mag.*, vol. 59, no. 4, pp. 88–94, Apr. 2021.

[33] R. E. Collin, *Antennas and Radiowave Propagation*.   McGraw-Hill, 1985.

[34] Y. Yang, M. Pesavento, S. Chatzinotas, and B. Ottersten, "Successive convex approximation algorithms for sparse signal estimation with nonconvex regularizations," *IEEE J. Sel. Topics Signal Process.*, vol. 12, no. 6, pp. 1286–1302, Dec. 2018.

[35] S. Boyd and L. Vandenberghe, *Convex Optimization*.   Cambridge University Press, 2004.

[36] A. S. Nemirovskii, "Interior point polynomial time methods in convex programming," Lecture notes, Faculty of Industrial Engineering and Management, Technion, The Israel Institute of Technology, 1994.

[37] S. G. Nash and A. Sofer, "On the complexity of a practical interior-point method," *SIAM J. Optim.*, vol. 8, no. 3, pp. 833–849, Aug. 1998.

[38] 3GPP TR 21.915 V15.0.0, Tech. Spec. Group Services and System Aspects, "5.5.4 radio physical layer aspects," Release 15, Sep. 2019.

[39] Z. Khan, H. Ahmadi, E. Hossain, M. Coupechoux, L. A. Dasilva, and J. J. Lehtomäki, "Carrier aggregation/channel bonding in next generation cellular networks: Methods and challenges," *IEEE Network*, vol. 28, no. 6, pp. 34–40, Nov.-Dec. 2014.

[40] https://www.lightreading.com/mobile/5g/china-mobile-huawei-claim-worlds-first-26ghz-4g-and-5g-integrated-network-demo-area/d/d-id/750747., May 2022.

[41] N. Goddemeier, D. Kai, and C. Wietfeld, "Role-based connectivity management with realistic air-to-ground channels for cooperative UAVs," *IEEE J. Sel. Areas Commun.*, vol. 30, no. 5, pp. 951–963, Jun. 2012.

[42] S. Jaeckel, L. Raschkowski, S. Wu, L. Thiele, and W. Keusgen, "An explicit ground reflection model for mm-Wave channels," in *Proc. Wireless Commun. Netw. Conf. Wrkshps.*, Mar. 2017, pp. 1–5.

[43] M. Giordani, M. Polese, A. Roy, D. Castor, and M. Zorzi, "A tutorial on beam management for 3GPP NR at mmWave frequencies," *IEEE Commun. Surveys Tuts.*, vol. 21, no. 1, pp. 173–196, 1st Quart. 2019.